17th World Conference on Earthquake Engineering, 17WCEE
Sendai, Japan - September 13th to 18th 2020

GROUND MOTION SIMULATION FOR THE 2014 M_w6.1 LUDIAN, CHINA EARTHQUAKE USING THE STOCHASTIC FINITE-FAULT METHOD

H. W. Wang[(1)], R. Z. Wen[(2)]

[(1)] *Harbin, P. R. China, Institute of Engineering Mechanics, China Earthquake Administration, whw1990413@163.com*
[(2)] *Harbin, P. R. China, Institute of Engineering Mechanics, China Earthquake Administration, ruizhi@iem.ac.cn*

Abstract

An M_w6.1 earthquake occurred in the Ludian County on 3 August 2014. The relocated aftershocks, and the inverted kinematic source rupture model indicated that it was a complex conjugated ruptured earthquake, containing two ruptured sections with NNW–SSE and ENE–WSW trending, respectively. A total of 200 kinematic source models of the Ludian event were stochastically constructed following the Graves and Pitarka method (Graves and Pitarka, 2015), which are characterized by the heterogeneous slip on the conjugated ruptured fault and slip-dependent spreading of the rupture front. Then, the stochastic finite-fault simulation method was applied to synthesize the horizontal ground acceleration seismograms produced by the M_w6.1 Ludian earthquake defined by various kinematic models. The heterogeneous slip plays a dominant role in the spatial distribution of ground motions, especially in the near-fault area. The peak ground accelerations (PGAs) and 5%-damped pseudospectral accelerations (PSAs) at short periods (< 0.5 s) estimated on the resulting synthetics generally math well with the observations at stations with Joyner-Boore distances greater than 20 km, while they are generally much lower than the predicted medians by BSSA14 model (Boore et al. 2014). The ground-motion variability caused by the complex source rupture process was further investigated by these synthetics. The standard deviations of PSAs on the base-10 logarithmic scale, i.e., Sigmalog_{10}(PSA), are closely dependent on either the spectral period or the Joyner-Boore distance. The Sigmalog_{10}(PSA) remains a constant approximately 0.55 at periods shorter than 0.1 s, and then increase continuously up to ~0.13 as the period increases from 0.1 to 2.0 s. The Sigmalog_{10}(PSA) values at periods of 0.1–2.0 s show the downward tendency as the Joyner-Boore distances increase. However, the Sigmalog_{10}(PSA) values at periods shorter than 0.1 s first decrease as the Joyner-Boore distances increase from ~1 km up to ~50 km, and then increase with the increasing Joyner-Boore distance.

Keywords: Ludian earthquake, ground motion simulation, stochastic source models, ground-motion variability

1. Introduction

An earthquake measured at M_s 6.5 by China Earthquake Network Center occurred in the northeast of the Yunnan province, close to the Ludian County, on 3 August 2014 at 16:30:20 (Beijing time). Its hypocenter is located at 27.109°N, 103.354°E at the depth of 15 km [1], and its moment magnitude was measured at M_w6.1 [2]. The focal mechanism solution indicated that the Ludian earthquake is a typical strike-slip event with the first nodal plane striking 162° and dipping 70° to WSW and the second nodal plane striking 257° and dipping 77° to NNW [2]. The aftershock relocations revealed that the Ludian earthquake sequence activated the intersection region of multiple faults, including the Zhaotong, Longshu, Dayandong, Baogunao, and Xiaohe faults (shown in Fig. 1). The surface projection of the relocated aftershocks are characterized by the spatial L-shaped distribution, consisting of two ~15-km-long sections with NNW–SSE and ENE–WSW trending, respectively [1, 2]. The epicenter of the Ludian earthquake is approximately located on the corner of the L-shaped aftershocks. The aftershocks primarily nucleated at the shallow crust with a depth of 4–16km [1, 3]. No significant surface rupture zone was observed during the field investigation immediately after the Ludian earthquake [4].

The seismogenic zone of the Ludian earthquake is located on the boundary between the active Sichuan–Yunnan rhombic block and the stable Yangtze Craton. The southeastward motion of the Sichuan–Yunnan block elucidated the frequent occurrence of earthquakes in this region. After the 21st century, the enhanced activity of the moderate earthquakes in this region has aroused special attention. In this region, the dense strong-motion observation network was installed and operated to collect the strong ground-motion recordings. During the Ludian earthquake, it obtained a total of 74 three-component ground motion recordings recorded by 70 free-field stations and 4 stations belonging to a structural observation array in Kunming [5]. These recordings were used in this study after uniform process using a Butterworth filter with a bandwidth of 0.5–30.0 Hz.

Considering the limited observation network and the lengthy recurrence period for large events, synthesis of ground motion in various approaches was an alternative way for predicting damages and losses from the future earthquake and evaluating ground-motion variability due to the complexity of earthquake source. In this study, the stochastic finite-fault method [6, 7] was performed to obtain the synthetic ground motions at a grid of 856 dummy stations in the study region (25.5°–28.5° N and 102°–104.5° E) produced by the M_w6.1 Ludian earthquake, of which a series of kinematic source models are stochastically generated.

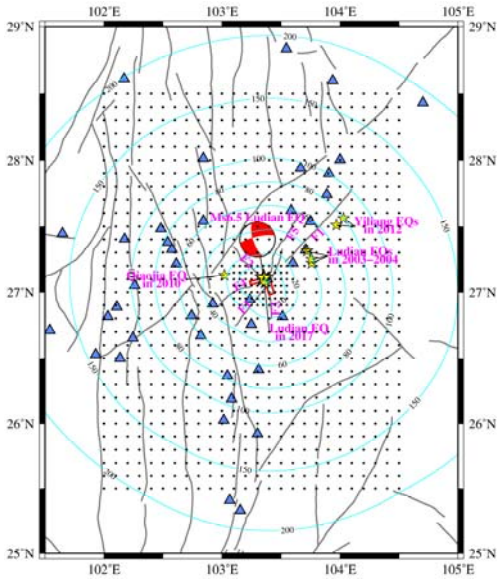

Fig. 1 – Location of the M_s6.5 Ludian earthquake in 2014. The triangles are the strong-motion stations recorded the Ludian event with Joyner-Boore distances smaller than 200 km. A series of moderate events

close to this event were marked by the stars. Gray lines indicate the faults in the study region, e.g., F1: Zhaotong fault, F2: Xiaohe fault, F3: Baogunao Fault, F4: Dayandong fault, F5: Longshu fault, etc. The rectangles represent the fault plane assumed in this study. Ground motions at 856 dummy stations (black dots) were simulated for the Ludian event.

2. Methodology and model parameters

The stochastic finite-fault method [6, 7] was applied to synthesize the ground motions produced by the M_w6.1 Ludian earthquake. Parameters accounting for the source, path, and site effects used for the simulations are summarized in Table 1.

The [8, 9, 10] method was implemented to generate kinematic rupture model with spatial heterogeneity in the slip distribution and slip-dependent spreading of the rupture front. A total of 200 realizations of kinematic source models were finally constructed for the Ludian earthquake. Fig. 2 shows four kinematic source models generated in this study for the subsequent simulation. The stress drop and pulsing percentage were set to 10 bar and 50% after multiple trial-calculation by varying stress drop and pulsing percentage values. The stress drop value applied in this simulation is approximately consistent to the estimate (i.e., 0.92 MPa) of Ludian event by [5].

Table 1 – Parameters used in ground motion simulations for the Ludian earthquake

Parameters	Representative values
Fault geometry (length × width)	NNW–SSE-trending fault: striking 162°, dipping 70° to WSW, length × width = 15 km × 13 km; ENE–WSW-trending fault: striking 257°, dipping 77° to NNW, length × width = 15 km × 13 km [2].
Initial rupture point and its position on fault	27.109°N, 103.354°E, and depth = 15 km [1]. NNW–SSE-trending fault: (0 km, 13 km); ENE–WSW-trending fault: (3 km, 13 km);
Seismic moment	Total: 1.58×10^{18} Nm (M_w = 6.1) [2]. NNW–SSE-trending fault: 0.79×10^{18} Nm. ENE–WSW-trending fault: 0.79×10^{18} Nm.
Stress drop	10 bars
Pulsing percentage	50% [7]
Slip distribution & Rupture process	200 realizations with heterogeneous slip distribution and slip-dependent rupture velocity generated stochastically using the [8, 9, 10] method
Shear-wave velocity (β)	3.55 km/s [11]
Density (ρ)	2.70 g/cm^3 [11]
Geometrical spreading	Empirical model developed by [12]
S-wave quality factor	$Q(f) = 180f^{0.5}$ [12]
Path duration	Empirical model applicable for the active tectonic regions developed by [13]
Crustal amplification	The amplification model for the NEHRP B/C boundary site [14]
Site amplification	The site-specific amplification function considered in the ground motion

	prediction models of [15]
High-frequency decay factor κ	0.025 s [12]

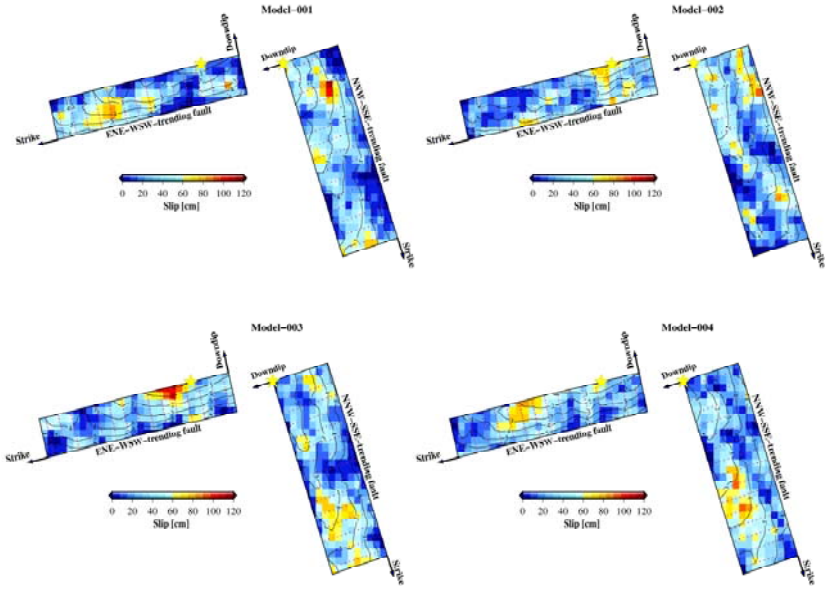

Fig. 2 – Four kinematic source models stochastically generated for the Ludian earthquake using the [8, 9, 10] method. The contours of the arrival of the rupture front at interval of 1 s are superposed upon the spatial distribution of the slip on the surface projection of the fault planes. The star indicates the epicenter of the Ludian event.

3. Resultant synthetics

The study region was divided into regular grids on a size of 0.1°×0.1°. However, the shrinking grids on a size of 0.05°×0.05° were considered within the limited near-fault area, in the range of 26.9°–27.2° N and 103.1°–103.55° E. The ground acceleration seismograms at single horizontal component were synthesized at a grid of 856 dummy stations (i.e., the purple dots in Fig. 1) with R_{JB} = 0.0–213.5 km by the stochastic finite-fault method based on each of the 200 random source models. The synthetic results were used to calculate the ground motion intensity measures, including the peak ground accelerations (PGAs), the peak ground velocities (PGVs), and the 5% damped pseudospectral accelerations (PSAs) at periods of 0.1–2.0 s. Meanwhile, we provided the mean values for these ground motion intensity measures on the base-10 logarithmic scale at each dummy station based on the 200 realizations of source models.

The mean values for both PGA and PGV on the base-10 logarithmic scale at a grid of 856 dummy stations were assembled to derive the contour maps, respectively, using the tension spline interpolation method, as shown in Fig. 3. The triangular contours for both the mean PGA and the mean PGV in the near-fault area are clearly observed and approximately in good agreement with the L-shaped surface projection of the fault plane. However, the contours for both the mean PGA and the mean PGV in areas far from the fault are draw approximately as the concentric circles sharing the epicenter as the center. These results reveal the key roles of the spatial state of ruptured fault exerting in the spatial distribution of the ground motions, on average, in the near-fault area. Moreover, the contour maps of the PGAs and PGVs estimated on the synthetics produced by the four random source models (Fig. 2) were also drawn in Fig. 3. These contours are rather irregular in shape compared with those accounting for the mean PGA and PGV. The distinctly various contours, especially in the near-fault area, come from the four random source models. Although the patches of the maximum PGA and PGV occur within the surface projection of the fault, the specific locations they

occupied differ from each other. It was further noticed that these patches are generally in good consistency with the areas with largest slip. These results clearly indicate the heterogeneous distribution in slip serves crucial roles in the spatial distribution of the resultant ground motions, especially in the near-fault area.

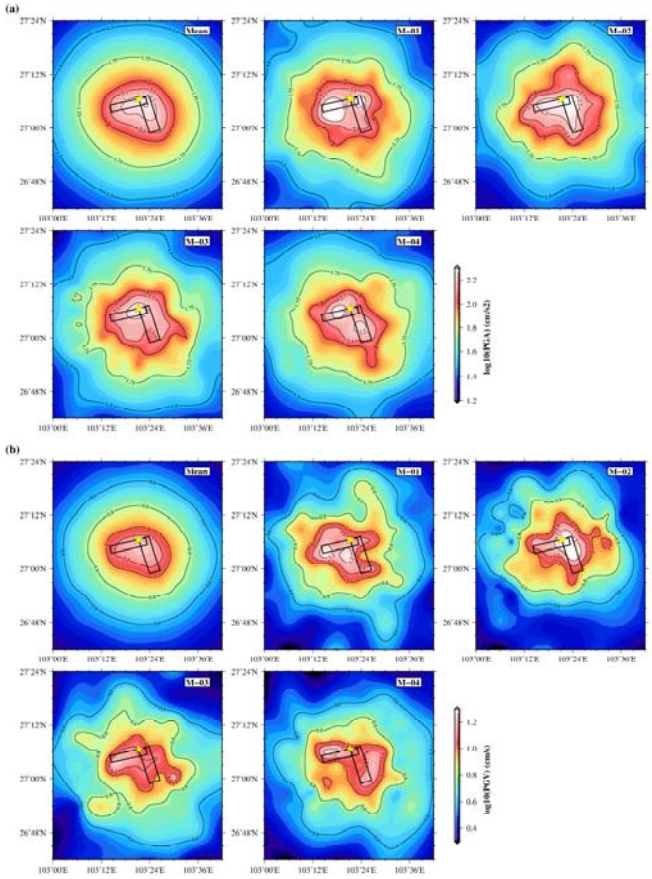

Fig. 3 – Spatial distribution of PGA (a) and PGV (b) values on the base-10 logarithmic scale estimated on the simulated ground motions. The contour maps for the mean PGA and PGV across all 200 source models were first provided, distinguished with 'Mean'. Contour maps of PGAs and PGVs resulting from the four random source models (M–01, M–02, M–03, and M–04) were followed.

The synthetic PGAs and PGVs were compared with the observations, i.e., the geometric means of both orthogonal horizontal components, as shown in Fig. 4 and the PSAs at periods of 0.1, 0.25, 0.5, 0.75, 1.0, and 1.5 s as shown in Fig. 5. The synthetic PGAs and the PSAs at short periods (0.1 and 0.25 s) generally math well with those recorded at stations with R_{JB} > 20 km. However, the overestimated PGVs and PSAs at periods of 0.5, 0.75, 1.0, and 1.5 s were generally provided for these stations. It was further noticed that such overestimation is getting worse as the distance increases, which may be interpreted by the slower path attenuation applied in the simulation. At the five near-fault dummy stations with R_{JB} = 0 km, the synthetic PGAs, PGVs, and PSAs were consistently underestimated to a great extent in comparison with observations at the only near-fault station (i.e., 053LLT). For example, the mean values for the synthetic PGAs and PGVs across the five dummy stations are 161.60 cm/s^2 and 13.90 cm/s respectively, far below the observations at 053LLT station (i.e., 800.36 cm/s^2 and 74.68 cm/s respectively).

The comparisons were also made through the predicted medians of ground motion intensity measures by BSSA14 model. The strike-slip fault type, M_w=6.1 and V_{s30} = 369.81 m/s were fixed and the regional adjustment of anelastic attenuation for China was considered in the BSSA14 model. However, the sediment thickness effects were not included due to the mountains area. Except for those recorded at 053LLT station, the predicted medians of PGAs, PGVs and PSAs were, in general, greater than those estimated on the synthesized and observed ground motions. Such overestimations gradually shrink as the spectral period

increases. The overall overestimation from the BSSA14 model during several strike-slip M_w~6.0 events in the western China has been confirmed by some recent studies, e.g., [5, 16]. The lower stress drop values for these events have been listed by [5], e.g., 0.92 MPa for the Ludian event, to explain the higher predictions of BSSA14 model, which represent the global events in the shallow crust with the higher value of the mean stress drop.

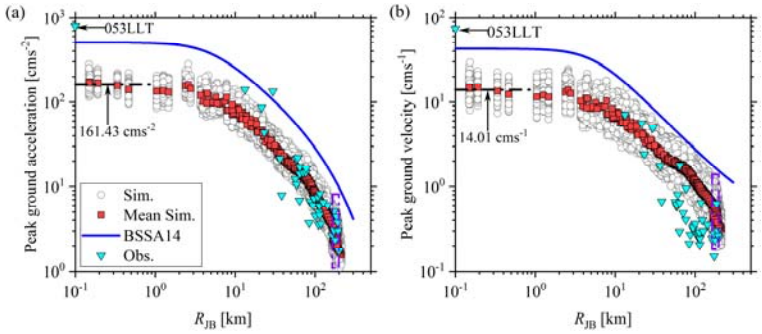

Fig. 4 – Peak ground accelerations (PGAs) (a) and peak ground velocities (PGVs) (b) estimated on the synthesized ground motions (circles), in comparison with medians predicted by the BSSA14 model (solid line) and the geometrical means of both orthogonal horizontal components of the observed recordings (triangle). The mean PGAs and PGVs across the resultant synthetics using the random source models are represented by the squares. The PGA and PGV recorded at 053LLT station with R_{JB} = 0 km are plotted on the vertical axis (i.e., R_{JB} = 0.1 km). The PGAs and PGVs of the synthetics at five dummy stations with R_{JB} = 0 km are plotted within the range of R_{JB} = 0.1–1.0 km.

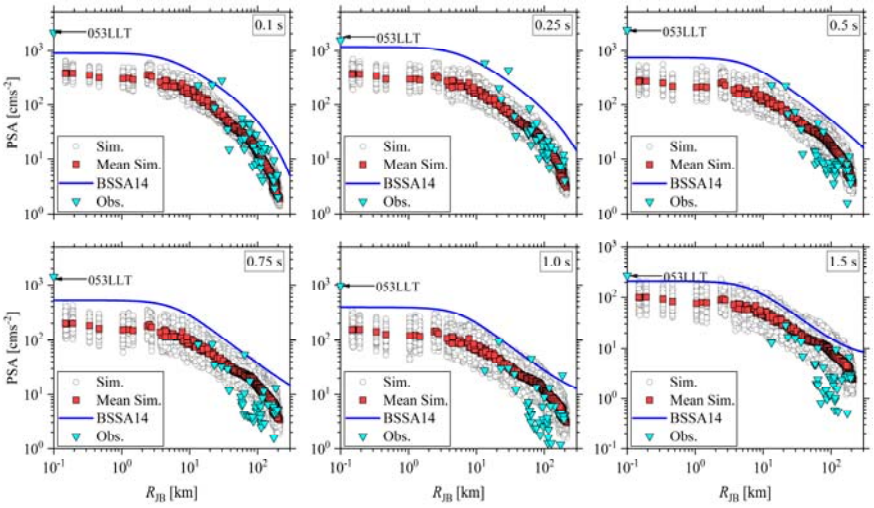

Fig. 5 – Same as Figure 4 but for pseudospectral accelerations (PSAs) at periods of 0.1, 0.25, 0.5, 1.0, 1.5, and 2.0 s, respectively.

4. Ground-motion variability

It has always been the hot concern to evaluate the variability of the ground motion caused by the uncertainty in the source rupture process, e.g., [17, 18, 19, 20, 21]. The standard deviations of the PSAs at periods of 0.05–2.0 s on the base-10 logarithmic scale (denoted as $\text{Sigma}_{\log10}$(PSA)) obtained from the simulated ground motions based on the random source models at each dummy station were calculated and plotted in Fig. 6. The close dependence of the $\text{Sigma}_{\log10}$(PSA) on either the spectral period or the R_{JB} appears to be observed. For example, the PSAs at dummy stations with R_{JB} < 5 km generally show the higher standard deviations.

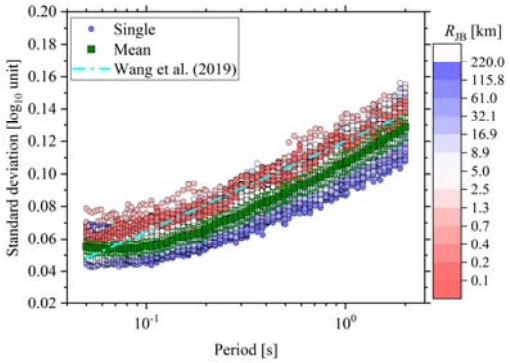

Fig. 6 – Standard deviation of the pseudospectral accelerations (PSAs) on the base-10 logarithmic scale from simulated ground motions using the random source models.

In order to clearly exhibit the potential dependence, the standard deviations of PSAs at several periods (0.05, 0.1, 0.5, and 1.0 s) against the R_{JB} values were shown in Fig. 7. The distance-binned means and standard deviations were shown in nine bins (1–10, 10–20, 20–30, 30–40, 40–50, 50–70, 70–100, 100–150, and 150–200 km). It can be seen that the standard deviations of PSAs at periods of 0.1, 0.5, and 1.0 s, in general, decrease gradually as the R_{JB} values increase. In a curious way, the standard deviations of PSAs at periods of 0.05 s first show the downward tendency as the distance increases from ~1 km up to ~50 km, while the upward tendency then dominants the larger distances. Similarly, [21] confirmed the considerable decrease for the ratios of the standard deviations of the PGAs and the PSAs at periods of 0.01–5 s between 20 and 50 km away from the fault. Considering the complexity of the source rupture process, [22] modeled the monotonous decay for the standard deviation of the PGV with the increasing distance as a power law relation, i.e., $\text{Sigma}_{\log10}(\text{PGV}) = aR_{JB}^{b}$. In this study, the power law relation was applied to describe the $\text{Sigma}_{\log10}$(PSA) dependent on R_{JB} (R_{JB} > 1 km included). It was capable of accounting for the dependence of the $\text{Sigma}_{\log10}$(PSA) values at periods of 0.1–2.0 s on R_{JB} since the high coefficients of determination (R^2), as shown in Fig. 8, were obtained from the linear least-square regression analysis. After further examinations, the relations between the $\text{Sigma}_{\log10}$(PSA) values at periods shorter than 0.1 s and R_{JB} are similar to that at period of 0.05 s (Fig. 7), which can not be described by the power law due to the small R^2 values (Fig. 8). Meanwhile, both regression coefficients, intercept a and slope b, were shown in Fig. 8, and the corresponding fitting curves were added in Fig. 7 for the four periods. The b values are consistently negative at periods of 0.1–2.0 s, which further verifies the downward tendency of the $\text{Sigma}_{\log10}$(PSA) with the distance increased. The period-dependent b values were obtained, which are characterized by the upward tendency with the increasing period from 0.1 to 2.0 s. This upward tendency reveals that the downward tendency of the $\text{Sigma}_{\log10}$(PSA) weakens gradually with the period increased. It is contrary to the results provided by [21], where the ratios of $\text{Sigma}_{\log10}$(PSA) values between 20 and 50 km away from the fault approximately increase as the period increases (i.e., the expanding downward tendency with the increasing period).

The upward tendency of the $\text{Sigma}_{\log10}$(PSA), as raised by some other studies (e.g., [17, 20]), were generally observed in Fig. 9 for some dummy stations (R_{JB} = 5.75, 24.24, 45.02, 85.73, 168.69 km, respectively) as the spectral period increases from 0.1 to 2.0 s. However, the $\text{Sigma}_{\log10}$(PSA) values are approximately constant at periods of 0.05–0.1 s. If the influence of R_{JB} is ignored, the $\text{Sigma}_{\log10}$(PSA) values at certain period obeys the Gaussian distribution (Fig. 7). The average $\text{Sigma}_{\log10}$(PSA) value over all dummy stations (squares in Fig. 6) remains constant, ~0.55, at periods of 0.05–0.1 s, and then persistently increase up to ~0.13 at periods of 2.0 s, generally lower than those provided by [20].

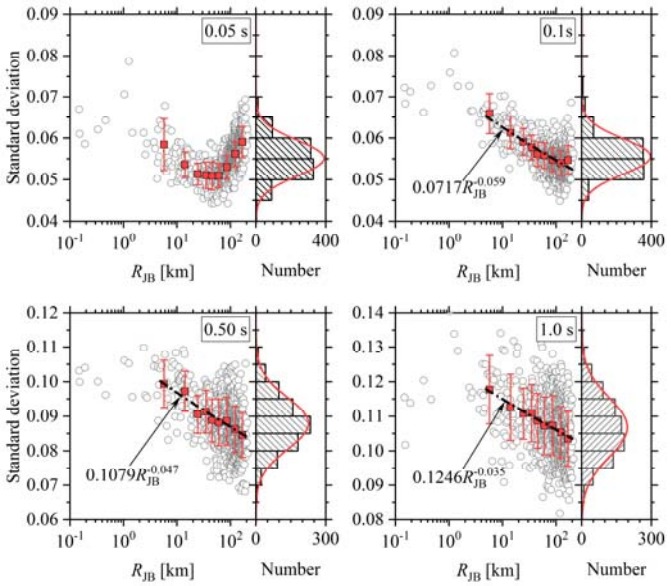

Fig. 7 – Standard deviations of PSAs at several periods (0.05, 0.1, 0.5, and 1.0 s) versus the Joyner-Boore distance (R_{JB}). The distance-binned means and standard deviations in nine bins are indicated by the squares and error bars, respectively. The dashed-dotted lines represent the best-fitting relation between the standard deviation and R_{JB}. Histograms of the standard deviations, and the best-fitting Gaussian distribution were provided. Standard deviations at the five dummy stations with R_{JB} = 0 km are plotted within the range of R_{JB} = 0.1–1.0 km.

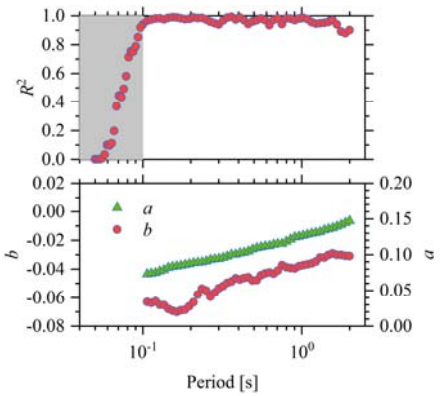

Fig. 8 – The coefficients of determination (R^2), slope b, and intercept a in the power law relation between the standard deviation of PSA and R_{JB} derived from the least-square regression analysis.

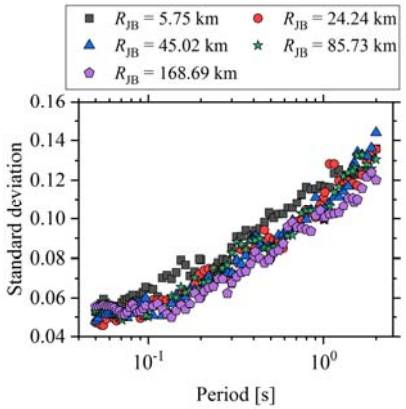

Fig. 9 – Standard deviations of PSAs at some dummy stations (R_{JB} = 5.75, 24.24, 45.02, 85.73, and 168.69 km) against the spectral periods from 0.1 to 2.0 s.

We further investigated the potential dependence of the $Sigma_{log10}$(PSA) on the azimuth of the dummy station. To this end, the $Sigma_{log10}$(PSA) values for each period in the range of 0.05–2.0 s were assembled at each of the five R_{JB} bins (10–30, 30–50, 50–70, 70–100, 100–150 km), and the means were calculated across the $Sigma_{log10}$(PSA) values within each R_{JB} bin at all considered periods. The $Sigma_{log10}$(PSA) values at each period within each R_{JB} bin were classified into 12 azimuth bins with a width of 15°. For each R_{JB} bin, we picked up the $Sigma_{log10}$(PSA) values at each period, greater than the mean for this R_{JB} bin, in each of the 12 azimuth bins. Then, the number of the selected $Sigma_{log10}$(PSA) values at all periods within each azimuth bin were used to calculate the proportion accounting for the total within the corresponding azimuth bin, as shown in Fig. 10. The larger proportion indicates the greater $Sigma_{log10}$(PSA) value in the azimuth bin. The strong dependence of the proportion on the azimuth was apparently observed for all R_{JB} bins. The polynomial curve with a single peak can be an ideal description for the proportion varied with azimuth. The peak proportion occurred at an azimuth of ~165°, approximately equal to the strike of the activated NNW–SSE-trending fault and also the forward direction of the rupture propagation.

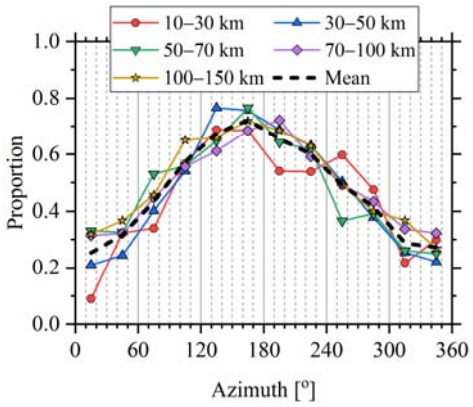

Fig. 10 – The proportion of the number of the selected $Sigma_{log10}$(PSA) values at all periods within each azimuth bin accounting for the total within the corresponding azimuth bin for the five R_{JB} bins. For each R_{JB} bin, the $Sigma_{log10}$(PSA) values at each period greater than the mean for the corresponding R_{JB} bin were picked up.

5. Conclusions

In this study, we applied the stochastic finite-fault method to synthesize the horizontal ground acceleration seismograms produced by the M_w6.1 Ludian earthquake on August 3, 2014 at a grid of 856 dummy stations. For this purpose, we developed a total of 200 kinematic source models for this Ludian event, which are characterized by the heterogeneous distribution in slip on the conjugated ruptured faults and slip-dependent spreading of the rupture front away from the hypocenter. The ground motion intensity measures, including PGA, PGV, and PSA, were estimated on the resultant synthetics. The spatial distributions of PGA and PGV indicate the crucial effects of the slip heterogeneity on ground motions, especially in the near-fault area. Moreover, the spatial state of the ruptured fault controls the spatial distribution of near-fault ground motion with the slip heterogeneity out of consideration. Using these input parameters listed in Table 1, PGAs and PSAs at short periods (< 0.5 s) estimated on the resulting synthetics generally math well with the observations at stations with R_{JB} > 20 km. However, the PGVs and PSAs at periods longer than 0.5 s were overestimated by these synthetics. Compared with the predicted medians of BSSA14 model, PGAs, PGVs, and PSAs obtained from synthetics were generally much smaller.

We further investigated the ground-motion variability caused by the complex source rupture process. The $Sigma_{log10}$(PSA) values are closely dependent on either the R_{JB} or the spectral period. The $Sigma_{log10}$(PSA) values at periods of 0.1–2.0 s show the downward tendency as the distance increases. This downward

tendency of the $Sigma_{log10}$(PSA) weakens gradually with the period increased. However, the $Sigma_{log10}$(PSA) values at periods lower than 0.1 s first decrease as the distance increases from ~1 km up to ~50 km, and then increase with the increasing distance. We inferred that the enlarged $Sigma_{log10}$(PSA) values at low periods at regional distances may be attributed to the basically random high-frequency properties introduced by the stochastic simulation method, which dominates the uncertainty of high-frequency motions after strong path attenuation. The $Sigma_{log10}$(PSA) remains a constant approximately 0.55 at periods smaller than 0.1 s, and then increase continuously up to ~0.13 as the period increases from 0.1 to 2.0 s. The $Sigma_{log10}$(PSA) values show the obvious dependence on the azimuth.

6. Acknowledgements

We contacted the email csmnc@iem.ac.cn for strong-motion recordings used in this article collected by the China Strong-Motion Network Center. This work was supported by the Science Foundation of the Institute of Engineering Mechanics, China Earthquake Administration (No. 2018B03), National Natural Science Foundation of China (No. 51808514).

7. References

[1] Wang WL, Wu JP, Fang LH, Lai GJ (2014): Double difference location of the Ludian Ms6.5 earthquake sequences in Yunnan province in 2014. *Chinese J. Geophys.* **57**, 3042–3051 (in Chinese).

[2] Zhang GW, Lei JS, Liang SS, Sun CQ (2014): Relocations and focal mechanism solutions of the 3 August 2014 Ludian, Yunnan Ms6.5 earthquake sequence. *Chinese J. Geophys*. **57**, 3018–3027 (in Chinese).

[3] Li YE, Chen XZ, Chen LJ, Guo XY (2015): Investigation on the rupture process of the Ludian Ms6.5 earthquake sequence in 3 August, 2014 in Yunnan province. *Chinese J. Geophys*. **58**, 3232–3238 (in Chinese).

[4] Xu XW, Jiang GY, Yu GH, Wu XY, Zhang JG, Li X (2014): Discussion on seismogenic fault of the Ludian Ms6.5 earthquake and its tectonics attribution. *Chinese J. Geophys.* **57**, 3060–3068 (in Chinese).

[5] Xu PB, Ren YF, Wen RZ, Wang HW (2019): Observations on regional variability in ground-motion amplitude from six Mw ~6.0 earthquakes of the North-South seismic zone in China. *Pure Appl. Geophys*. https://doi.org/10.1007/s00024-019-02176-6.

[6] Atkinson GM, Assatourians K (2015): Implementation and validation of EXSIM (a stochastic finite-fault ground-motion simulation algorithm) on the SCEC broadband platform. *Seism. Res. L*. **86**, 48–60.

[7] Motazedian D, Atkinson GM (2005): Stochastic finite-fault modeling based on a dynamic corner frequency. *Bull. Seism. Soc. Am*. **95**, 995–1010.

[8] Graves RW, Pitarka A (2010): Broadband ground-motion simulation using a hybrid approach. *Bull. Seism. Soc. Am.* **100**, 2095–2123.

[9] Graves RW, Pitarka A (2015): Refinements to the Graves and Pitarka (2010) broadband ground-motion simulation method. *Seism. Res. L.* **86**, 75–80.

[10] Graves RW, Pitarka A (2016): Kinematic ground-motion simulations on rough faults including effects of 3D stochastic velocity perturbations. *Bull. Seism. Soc. Am.* **106**, 2136–2153.

[11] Laske G, Masters G, Ma Z, Pasyanos M (2013): Update on CRUST1.0: a 1-degree global model of Earth's crust. Geophysical Research Abstract, 15, Abstract EGU2013-2685, http://igppweb.ucsd.edu/~gabi/crust1.html.

[12] Xu Y, Herrmann RB, Wang C-Y, Cai S (2010): Preliminary high-frequency ground-motion scaling in Yunnan and Southern Sichuan, China. *Bull. Seism. Soc. Am*. **100**, 2508–2517.

[13] Boore DM, Thompson EM (2014): Path durations for use in the stochastic-method simulation of ground motion. *Bull. Seism. Soc. Am*. **104**, 2541–2552.

[14] Atkinson GM, Boore DM (2006): Earthquake ground-motion prediction equations for eastern North America. *Bull. Seism. Soc. Am.* **96**, 2181–2205.

[15] Boore DM, Stewart JP, Seyhan E, Atkinson GM (2014): NGA-West2 equations for predicting PGA, PGV, and 5% damped PSA for shallow crustal earthquakes. *Earthq. Spectra* **20**, 1057–1085.

[16] Ren YF, Wang HW, Xu PB, Dhakal YP, Wen RZ, Ma Q, Jiang P (2018): Strong-motion observations of the 2017 Ms7.0 Jiuzhaigou earthquake: comparison with the 2013 Ms7.0 Lushan earthquake. *Seism. Res. L.* **89**, 1354–1365.

[17] Causse M, Cotton F, Cornou C, Bard P-Y (2008): Calibrating median and uncertainty estimations for a practical use of empirical Green's functions technique. *Bull. Seism. Soc. Am.* **98**, 344–353.

[18] Kaneko Y, Shearer PM (2014): Seismic source spectra and estimated stress drop derived from cohesive-zone models of circular subshear rupture. *Geophys. J. Int.* **197**, 1002–1015.

[19] Kaneko Y, Shearer PM (2015): Variability of seismic source spectra, estimated stress drop, and radiated energy, derived from cohesive-zone models of symmetrical and asymmetrical circular and elliptical ruptures. *J. Geophys. Res. - Sol. Earth* **120**.

[20] Wang HW, Ren YF, Wen RZ, Xu PB (2019): Investigating the contribution of stress drop to ground-motion variability by simulations using the stochastic empirical Green's function method. *Pure Appl. Geophys*. 176, 4410–4435.

[21] Crempien JGF, Archuleta RJ (2017): Within-event and between-events ground motion variability from earthquake rupture scenarios. *Pure Appl. Geophys.* **174**, 3451–3465.

[22] Vyas JC, Mai PM, Galis M (2016): Distance and Azimuthal dependence of ground-motion variability for unilateral strike-slip ruptures. *Bull. Seism. Soc. Am.* **106**, 1584–1599.

